 Q. J. R. Meteorol. Soc. 143: 1434–1441, April 2017 A DOI:10.1002/qj.3015

RMetS
Royal Meteorological Society

Characteristics of colliding sea breeze gravity current fronts: a laboratory study

Karin van der Wiel,[a,b]* Sarah T. Gille,[c] Stefan G. Llewellyn Smith,[c,d] P. F. Linden[e] and Claudia Cenedese[f]

[a]*Centre for Ocean and Atmospheric Sciences, University of East Anglia, Norwich, UK*
[b]*Atmospheric and Oceanic Sciences, Princeton University, NJ, USA*
[c]*Scripps Institution of Oceanography, University of California San Diego, La Jolla, USA*
[d]*Department of Mechanical and Aerospace Engineering, University of California San Diego, La Jolla, USA*
[e]*Department of Applied Mathematics and Theoretical Physics, University of Cambridge, UK*
[f]*Woods Hole Oceanographic Institution, MA, USA*

*Correspondence to: K. van der Wiel, now at: Royal Netherlands Meteorological Institute, Postbus 201, 3730 AE, De Bilt, Netherlands. E-mail: wiel@knmi.nl

Sea and land breeze circulations driven by surface temperature differences between land and sea often evolve into gravity currents with sharp fronts. Along narrow peninsulas, islands and enclosed seas, sea/land breeze fronts from opposing shorelines may converge and collide and may initiate deep convection and heavy precipitation. Here we investigate the collision of two sea breeze gravity current fronts in an analogue laboratory setting. We examine these collisions by means of 'lock-exchange' experiments in a rectangular channel. The effects of differences in gravity current density and height are studied. Upon collision, a sharp front separating the two currents develops. For symmetric collisions (the same current densities and heights) this front is vertical and stationary. For asymmetric collisions (density differences, similar heights) the front is tilted, changes shape in time and propagates in the same direction as the heavier current before the collision. Both symmetric and asymmetric collisions lead to upward displacement of fluid from the gravity currents and mixing along the plane of contact. The amount of mixing along the collision front decreases with asymmetry. Height differences impact post-collision horizontal propagation: there is significant propagation in the same direction as the higher current before collision, independent of density differences. Collisions of two gravity current fronts force sustained ascending motions which increase the potential for deep convection. From our experiments we conclude that this potential is larger in stationary collision fronts from symmetric sea breeze collisions than in propagating collision fronts from asymmetric sea breeze collisions.

Key Words: sea breeze; land breeze; gravity current; convergence; deep convection; GFD; fluid dynamics

Received 22 June 2016; Revised 27 January 2017; Accepted 1 February 2017; Published online in Wiley Online Library 20 April 2017

1. Introduction

Differences in the heating of air over the land and the sea create horizontal density differences that set up atmospheric circulations. These circulations, referred to as the sea or land breeze, occur in many coastal regions and are examples of atmospheric gravity currents. Gravity currents, or buoyancy-driven currents, are flows along a boundary driven by horizontal density differences under the influence of a gravitational field (Simpson, 1997; Miller *et al.*, 2003).

Sea/land breeze development is influenced by many meteorological and environmental factors, including the land–sea surface temperature difference, atmospheric stability, orography, the curvature of the local coast and large-scale meteorological conditions (Miller *et al.*, 2003). Ahead of a sea breeze front, ascending motions of the order $1-2\,\mathrm{m\,s^{-1}}$ are found (Simpson, 1969; Helmis *et al.*, 1987; Moncrieff and Liu, 1999). The horizontal extents of sea/land breezes depend strongly on latitude, as closer to the Equator the solar insolation is stronger and the Coriolis force due to the rotation of the Earth is less (e.g. Niino, 1987; Yan and Anthes, 1987; Tijm *et al.*, 1999; Miller *et al.*, 2003). In England (50°N) and the Netherlands (52°N), sea breeze fronts have been observed 100 km inland (Simpson *et al.*, 1977; Tijm *et al.*, 1999), while in southern Australia (32°S) fronts can travel as far as 400 km from the coast (Clarke, 1983).

These large inland penetrations mean that, for narrow peninsulas or islands, sea breezes from opposing shorelines can interact. Observational case-studies and numerical model experiments for locations around the world have shown that

such convergences are widespread. Known examples of sea breeze convergence include: Florida, USA (Byers and Rodebush, 1948; Pielke, 1974; Burpee, 1979; Nicholls *et al.*, 1991), the Cape York Peninsula, Australia (Noonan and Smith, 1986), Mallorca, Spain (Ramis *et al.*, 1990; Sumner *et al.*, 1993), the Tiwi islands, Australia (Carbone *et al.*, 2000; Crook, 2001), Salento, Italy (Mangia *et al.*, 2004) and Cornwall, England (Golding, 2005). Land breeze convergence has been shown to occur over the North American Great Lakes (Forbes and Merritt, 1984; Niziol *et al.*, 1995), between the Tiwi islands and Australia (Wapler and Lane, 2012) and, based on global satellite measurements, Gille *et al.* (2003) show that such convergences can be expected over any body of water narrower than 500 km. Gille and Llewellyn Smith (2014) note that for enclosed seas, wind phase lines converge at gravity-wave propagation speeds, which are faster than the propagation speeds of land breeze fronts. For convenience, we will refer to both sea and land breezes as 'sea breezes' in the remainder of this article.

For sea breeze convergences, the horizontal propagation speed is probably the most important factor in determining how far inland a front travels and whether a collision will occur. This speed is most significantly influenced by (i) the magnitude of the surface temperature difference between land and sea and (ii) the strength and direction of the ambient wind (e.g Arritt, 1993; Tijm *et al.*, 1999; Gahmberg *et al.*, 2010; Warren, 2014). In turn, the temperature difference is mostly a function of the surface sensible heat flux into the ground. Here it will be assumed that the conditions to create a collision are met, and the main focus will be on the collision event. Factors influencing the density, the propagation speed or the height of the sea breeze after its formation (e.g. Robinson *et al.*, 2013) will therefore be neglected.

In operational weather forecasting, increasing the predictive skill of severe weather conditions is important. For local communities, knowing both the time and location of extreme events with substantial advance warning is crucial (Wilson *et al.*, 1998; Browning *et al.*, 2007; Wulfmeyer *et al.*, 2011). Many previous studies on the convergence and collision of two sea breeze fronts are case-studies based on either observational data or numerical experiments. Most of these studies show that these collisions lead to an enhancement of ascending motion, deep convection and precipitation (e.g. Byers and Rodebush, 1948; Forbes and Merritt, 1984; Blanchard and López, 1985; Noonan and Smith, 1986; Nicholls *et al.*, 1991; Sumner *et al.*, 1993; Fankhauser *et al.*, 1995; Carbone *et al.*, 2000; Crook 2001; Golding, 2005; Wapler and Lane, 2012; Warren, 2014; Rizza *et al.*, 2015). Sea breeze convergence may also lead to enhanced air pollution (Mangia *et al.*, 2010). The timing and location of the collision and its heaviest impacts depend on many factors including the curvature of coastlines, topographic features, soil moisture levels and the presence of land breezes prior to sea breeze development (Baker *et al.*, 2001).

We highlight two idealized numerical studies that have systematically investigated specific aspects of the sea breeze convergence. Xian and Pielke (1991) show that maximum ascending motions are triggered over land masses of 100–150 km width; narrower land masses do not allow the development of a mature sea breeze circulation, collisions over wider land masses generally occur after sunset and consequently have weaker convergence. Warren (2014) shows that the collision of more developed sea breezes (increased propagation speeds and increased heights) displace more air mass in the vertical than weaker sea breezes. Factors that are shown to impact vertical air displacement, in order of influence, are: surface heat flux, atmospheric mixed-layer depth and atmospheric stability. Latitude and land surface roughness are shown to have less influence. Furthermore, ambient wind strength and direction, and coastal curvature are shown to influence the strength of convergence and, if a collision happens, its location.

Besides sea breezes, convective outflows also take the form of gravity currents (Simpson, 1997). Outflow currents are formed by downdraughts from thunderstorms; evaporative cooling in the thunderstorms creates the cold, dense air of the gravity current. Collisions of two of such outflow currents, or collisions between an outflow and a sea breeze front may initiate convection in a way similar to collisions of two sea breeze fronts (e.g. Droegemeier and Wilhelmson, 1985; Wilson and Schreiber, 1986; Carbone *et al.*, 1990; Kingsmill, 1995; Moncrieff and Liu, 1999; Banacos and Schultz, 2005; Soderholm *et al.*, 2015).

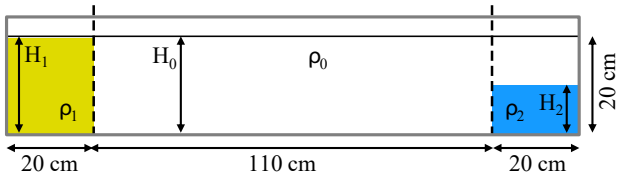

Figure 1. Sketch of the experimental setup. Symbols are defined in the text. [Colour figure can be viewed at wileyonlinelibrary.com].

In this study, we present laboratory experiments designed to examine the collision of two gravity currents. Such experiments provide a way to investigate these collisions in a controlled setting, and to extend the knowledge from field campaigns, observational and numerical studies. There have been many experimental studies on gravity currents (e.g. Britter and Simpson, 1978; Hacker *et al.*, 1996; Simpson, 1997; Shin, 2001; Maxworthy *et al.*, 2002; Shin *et al.*, 2004; Cenedese and Adduce, 2008; Dai, 2013); however few previous studies have considered two colliding gravity currents. Simpson (1997) showed the emergence of two bores travelling in opposite directions after a collision. Shin (2001) presented experimental results based on collisions of currents of equal density but different heights and developed a theory based on momentum and energy conservation that predicts the propagation speed of the bores formed as a result of the collision.

The novelty of the experiments described in this article lies in examining the influence of both height differences and density differences between the colliding fronts, thus expanding on the earlier experimental work of Shin (2001). Height and density are two of the key parameters that vary in environmental sea breeze convergences and which have been shown to impact the strength of the collision (Warren, 2014). In the natural environment, density differences in sea breezes may be created by differing sea-surface temperatures on opposing coasts. In convective outflows the rate of evaporative cooling determines the outflow density. Height differences may be expected in the natural environment in the collision of sea breeze fronts and convective outflows, or in the collision of two outflow currents. We restrict the analysis to the two-dimensional case which is relevant since many sea breeze circulations produce relatively straight fronts. The experiments are described in section 2. Experimental results are illustrated in section 3. The conclusions are discussed in section 4.

2. Experimental description

For this study gravity currents were created in a laboratory tank by means of 'lock exchange' experiments, in which fluids of different density were initially at rest and separated by a vertical barrier. Once the barrier was removed, the denser fluid flowed along the bottom of the tank into the lighter, ambient fluid.

The experiments were carried out in a horizontal rectangular glass channel, 150 cm long and 15.5 cm wide (Figure 1). In all experiments the channel was filled to a depth of $H_0 = 20$ cm. The tank was illuminated from behind using a uniform light sheet, and the experiments were filmed using a video camera located approximately 2 m from the tank.

At each end of the tank a separate section, or 'lock', was made using a vertical barrier, or 'lock gate' (dashed lines in Figure 1). The locks were 20 cm long. In the locks salt (NaCl) was added to the water to increase the density and thus create the horizontal density differences needed for the gravity currents. Yellow and blue food dyes were added to distinguish the denser fluids from the transparent, fresh, ambient fluid. Densities were measured with an accuracy of 5×10^{-5} g cm^{-3} using an Anton Paar DMA 58 densitometer.

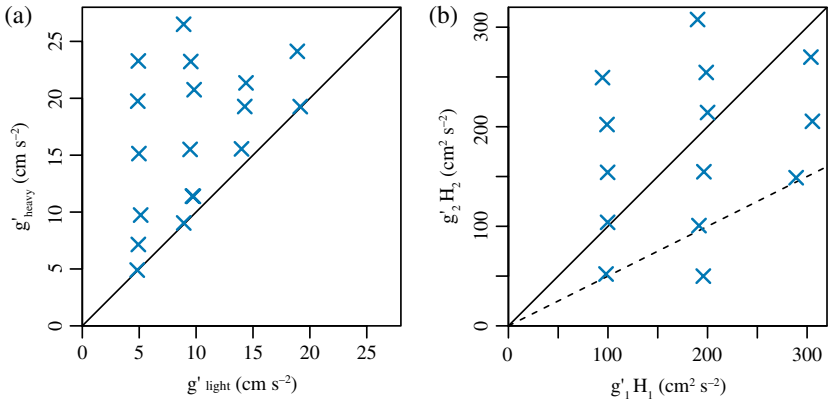

Figure 2. Positions in parameter space of the experiments. (a) Full-depth experiments, with diagonal line indicating the symmetric case in which $g'_{\text{light}} = g'_{\text{heavy}}$. (b) Half-depth experiments, with the solid diagonal line indicating symmetry and the dashed line indicating equal g'. [Colour figure can be viewed at wileyonlinelibrary.com].

Two sets of experiments were performed. The first set was designed to study the influence of (relative) differences in density on the collision. This set of experiments will be referred to as 'full-depth' lock exchanges or 'full-depth' experiments. Both locks were filled to the top with dense fluid, i.e. $H_1 = H_2 = H_0$, where H_1 and H_2 are the heights of denser fluids in the two locks. The density in the locks are denoted by ρ_1 and ρ_2, respectively (Figure 1). In total 18 full-depth experiments were conducted.

In the second set of experiments the depth of *one* of the locks was half of the total depth ($H_1 = H_0$, $H_2 = H_0/2$; Figure 1). This set of experiments will be referred to as 'half-depth' experiments. A second independent parameter, the gravity current height, was introduced to the problem this way. In total 14 half-depth experiments were conducted.

At the beginning of each experiment, the lock gates were pulled up simultaneously. The propagation speeds of the gravity currents were found by image analysis of the experimental videos. The position of the front was mapped in time, and a linear regression line was fitted. Soon after the release, the gravity currents entered the constant-speed regime (Rottman and Simpson, 1983), and the collision event happened within this regime. The Reynolds number of the currents always exceeds 3500 and thus viscous effects are negligible (Simpson, 1997, p. 141).

The dimensionless horizontal propagation speed of a gravity current generated from a lock exchange is given by the Froude number,

$$F_H = \frac{U}{\sqrt{g'H}}, \tag{1}$$

where g' is the reduced gravity, H is the height of the dense fluid in the lock and U the horizontal propagation speed (Simpson, 1997). The reduced gravity is the buoyancy between the gravity current of density ρ and the ambient fluid of density ρ_0, defined by

$$g' \equiv g\frac{\rho - \rho_0}{\rho_0}, \tag{2}$$

where g is the gravitational acceleration. In the remainder of this article, g'_1 will be used to refer to the reduced gravity of the current with H_1 and ρ_1, and g'_2 will be used to refer to the reduced gravity of the current with H_2 and ρ_2. In the experiments the values of $g'_1, g'_2 < 30\,\text{cm}\,\text{s}^{-1}$ (Figure 2(a)), so that density differences are less than 3%, and the flows can be considered as Boussinesq.

Borden and Meiburg (2013) provide an overview of Froude number predictions. Although there are different predictions of the Froude number, we use the expression by Shin *et al.* (2004) which is the only one that applies to both full-depth and partial-depth lock releases, and gives

$$F_H = \frac{\sqrt{2 - H/H_0}}{2}. \tag{3}$$

We note that the Shin *et al.* (2004) solution provides a closed-form analytic solution and is therefore based on a number of assumptions and physical simplifications. Numerical experiments may provide more detail on key physical processes. In the analysis of the results, we assume the currents are two-dimensional, and effects in the third lateral cross-channel dimension are ignored.

All experiments are mapped in parameter space in Figure 2. For the full-depth experiments (Figure 2(a)), the ratio of the reduced gravities of the lighter (g'_{light} = lower of g'_1 and g'_2) and the denser (g'_{heavy} = higher of g'_1 and g'_2) gravity currents,

$$r_g \equiv \frac{g'_{\text{light}}}{g'_{\text{heavy}}}, \tag{4}$$

ranged over $0.21 < r_g < 0.99$. For the half-depth experiments (Figure 2(b)) this ratio ranged over $0.19 < r_g < 0.97$.

3. Experimental results

Snapshots from two full-depth and half-depth experiments are shown in Figures 3 and 4, respectively. Figure 3(a) shows a symmetric case, where g'_{light} was almost equal to g'_{heavy} ($r_g = 0.99$), and Figure 3(b) is a full-depth asymmetric case with the heavier fluid dyed blue (propagating from the right, $r_g = 0.33$). Figure 4(a) shows the collision between two currents with $r_g = 0.95$ but different heights, while in Figure 4(b) an experiment with two currents having approximately equal $g'H$ is shown (different g', different H). The associated videos are included as supplementary movies online.

The propagation of the gravity currents before collision (Figures 3 and 4, second row) will be discussed in section 3.1 and compared to the theoretical prediction (Eq. (3)). The collision will then be analysed in more detail. In particular, the shape and propagation speed of the collision front will be considered. Due to mixing of the two dyed fluids and the ambient fluid upon collision, it is not possible to measure vertical velocities in the current experimental set-up to a satisfactory accuracy, and hence these will not be discussed further. The shape of the collision front (Figures 3 and 4, third row) will be discussed from a qualitative standpoint. The maximum vertical displacement (Figures 3 and 4, fourth row) and the horizontal propagation speed of the collision front will be investigated quantitatively. The vertical displacements at the collision front will be discussed in section 3.2. Horizontal propagation of the collision front and mixing along the collision front will be discussed in section 3.3.

3.1. *Pre-collision gravity current propagation speed*

The fronts of the gravity currents were observed to travel at a constant speed until they collided. Figure 5 compares the measured Froude numbers of the gravity currents (Eq. (1)) with

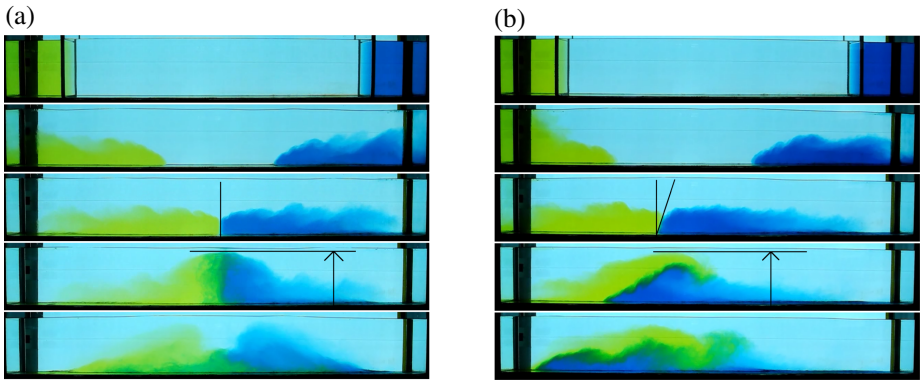

Figure 3. Snapshots of two full-depth experiments at different times. Note that the time difference between different panels is not the same for the two experiments. (a) Symmetric case with $r_g = 0.99$, (b) asymmetric case with $r_g = 0.33$. Top: initial set-up, second row: pre-collision gravity currents, third row: initial collision, fourth row: maximum collision height, bottom: post-collision. [Colour figure can be viewed at wileyonlinelibrary.com].

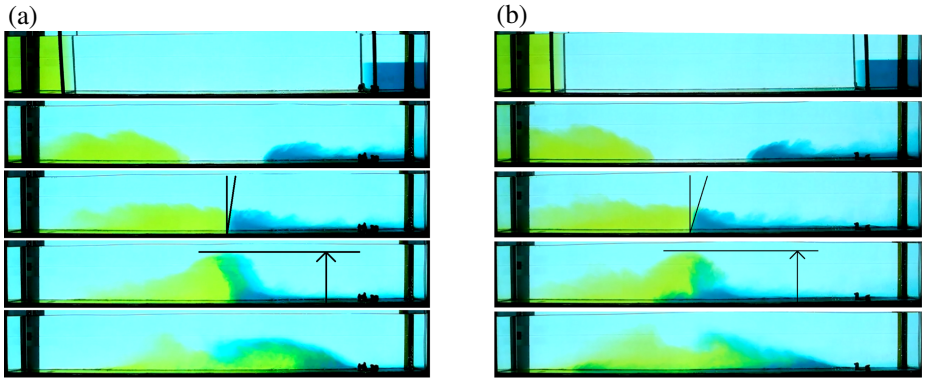

Figure 4. As Figure 3, but now for two half-depth experiments. (a) Case with approximately equal g' ($r_g = 0.95$), (b) case with approximately equal $g'H$ ($r_g = 0.48$). [Colour figure can be viewed at wileyonlinelibrary.com].

the theoretical prediction (Eq. (3)). The theoretical prediction for a dissipationless current (Eq. (3)) is plotted for both full-depth and half-depth lock heights (lines in Figure 5). Lower lock heights create slower propagating gravity currents with a higher Froude number. The observed Froude numbers are about 15% lower than the theoretical values, independent of the value of g' or the height H of the dense fluid in the lock, which is consistent with previous measurements of gravity current speeds (e.g. the summary in Shin *et al.*, 2004). For the full-depth experiments we find a mean Froude number of 0.42 instead of the theoretical prediction of 0.5. The mean Froude number for the half-depth experiments is 0.53, where theory predicts 0.61. These reductions from the predicted Froude numbers are mainly a result of energy loss associated with mixing with the ambient fluid due to shear instabilities along the top of the current (Hughes and Linden, 2016) rather than frictional energy losses.

3.2. *Collision shape and vertical displacement*

Figure 6 shows the two collision events in Figure 3 (third row) in more detail. Individual frames from the experimental videos were analysed to find the positions of the fronts in time. Depending on the shape of the front, rows or columns of pixels in the image were analysed using a threshold value of light intensity to find the front position. Both sequences start at time $\tau = 0$, which is the frame at which the fronts collide. Subsequent frames are separated by increments of 0.15 non-dimensional time units $\tau \equiv t/\sqrt{H_0/g_1' + H_0/g_2'}$. The figures show a short period of time ((a) $t = 1.3$ s and (b) $t = 2.1$ s) centred around the time corresponding to the third row of Figure 3. In the symmetric case, horizontal rows were analyzed to locate the front position; therefore the top of the currents is not detected in the last four panels of Figure 6(a).

In the symmetric case of equal g' (Figure 6(a)) the shapes of the individual gravity current fronts are essentially the same, and the collision front is vertical. In time this front extends in height and remains vertical. Mixing occurs along the collision line as can be seen by the presence of green dye resulting from the mixing of the blue and yellow dyes in the two currents. The asymmetric case is different (Figure 6(b)). The individual gravity current fronts change shape as they approach each other and therefore have different steepnesses upon collision. The collision front develops at an angle with the heavier dense fluid (blue, right) intruding underneath the lighter dense fluid (yellow, left). The front shape is not steady in time. At $\tau = 0.30$ a new gravity current forms at the bottom, and Kelvin–Helmholtz billows develop at the top of the denser (blue) current (Sha *et al.*, 1991). The front shape evolves from an initial angled straight line to an S-shaped front that changes shape to become more horizontal with increasing time. The angle from the vertical at which the collision front forms (denoted in the third row of Figure 3 and at $\tau = 0.15$ in Figure 6) is zero for symmetric collisions (vertical front) and increases with increasing asymmetry between the colliding fronts (tilted front).

As a direct consequence of the ascending motions forced by the collision event, dyed fluid is displaced vertically. The energy-conserving theory of Shin *et al.* (2004) predicts that, before collision, the heights of the gravity currents is equal to half the lock depth, i.e.

$$h = \frac{1}{2}H_i, \qquad i = 1, 2. \tag{5}$$

The heights of the individual gravity currents from full-depth lock releases (light pink and green marks in Figure 7(a) and light pink marks in Figure 7(b)) agree with these theoretical values (light pink and green lines in Figure 7(a) and light pink line in Figure 7(b)). There is a discrepancy between the measured and predicted height of the current for the half-depth lock releases.

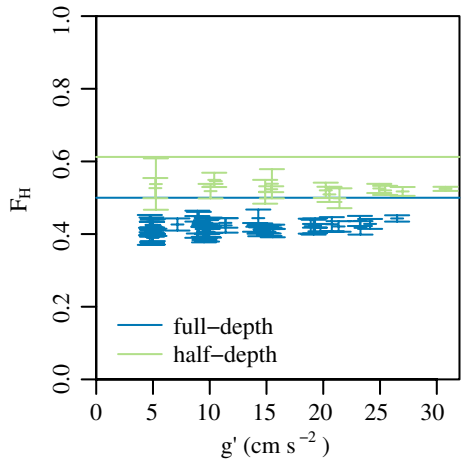

Figure 5. Froude numbers versus reduced gravity. Marks are individual experiments, lines are the theoretical values based on Eq. (3). Error bars show the range of Froude numbers measured for each current. The dark blue marks and line correspond to the full-depth experiments and light green marks and line to the half-depth experiments. [Colour figure can be viewed at wileyonlinelibrary.com].

This discrepancy may be caused by the limited length of the lock in the current experimental set-up or by the assumptions that were made in the theoretical model. Further experiments with a numerical model could be used to investigate the cause of the difference between experiment and theory.

After collision, the maximum height of the dyed fluids in the full-depth experiments is approximately 0.90 of the total water depth, independent of r_g (dark blue marks in Figure 7(a)) or pre-collision propagation speeds (not shown). The half-depth experiments (Figure 7(b)) show more variation in collision height, although no systematic trends can be inferred. Despite there being two significantly different lifting processes, the maximum collision height is observed to be comparable, independent of the dominant lifting process.

Based on the small spread of maximum heights in the data and the corresponding error bars, it is difficult to determine the role of gravity current height, density and speed. For all experiments, the maximum height of the fluid raised in the collision is a significant fraction of the total fluid depth, and it is possible that the presence of the free surface has an influence on the vertical motion near the top of the rising dense fluid.

3.3. *Horizontal propagation of the collision front*

Figures 3(a) and 6(a) show that in the full-depth symmetric case the collision front is stationary. There is some mixing, but the front does not move horizontally from the point of impact. In the asymmetric case the heavier gravity current (dyed blue, propagating from the right) continues propagating in its original direction (Figures 3(b) and 6(b)). In Figure 8, Hovmöller diagrams for three full-depth experiments are shown. These have been created by selecting a horizontal line one pixel thick along the bottom of the tank and stacking consecutive frames. The colour in these figures is the same as in Figures 3 and 6. The constant speeds of the two fronts before collision are shown by the straight edges to the yellow and blue regions at early times. The speeds of the individual currents essentially do not change prior to the point of impact.

The symmetric case confirms earlier observations; the individual gravity currents propagate at equal speeds toward each other, and upon collision mixing occurs. There is no evidence of further horizontal propagation of the collision front, and a growing mixed region develops between the now stationary currents, as can be seen from the green striated region from $t > 5$ s in Figure 8(a). In the strongly asymmetric case (Figure 8(b); $r_g = 0.33$) the heavier current (dyed blue, propagating from the right) continues to propagate in the same direction with a slightly reduced speed after collision. The flow of the lighter (yellow) current above the heavier (blue) current is not captured in this plot. Again there is mixing along the collision front that increases with time after impact. A third experiment with a weaker asymmetry ($r_g = 0.61$) is shown in Figure 8(c). Similar to the previous experiment, the collision front propagates in the direction of the propagation of the heavier current, but in this case the heavier (blue, right) current is significantly slower after collision. The mixing along the front of the heavier current is greater, as inferred from the size of the green region, than in the more strongly asymmetric case (Figure 8(b)).

The horizontal propagation speed of the heavier current after collision has been measured for all full-depth experiments. In Figure 9 these measured post-collision front speeds are plotted against the characteristic speed associated with the density difference between the two currents:

$$\sqrt{g_c' H_0}, \tag{6}$$

with the reduced gravity g_c' based on the densities of the two interacting currents:

$$g_c' = g\,\frac{\rho_{\text{heavy}} - \rho_{\text{light}}}{\rho_0}. \tag{7}$$

The near-symmetric collisions ($r_g > 0.89$; light green marks in Figure 9) create stationary fronts, as can also be seen in Figures 3(a), 6(a) and 8(a). The characteristic speed (Eq. (6)) is low but positive for these cases, indicating slow propagation of the collision front. In the experiments, mixing along the

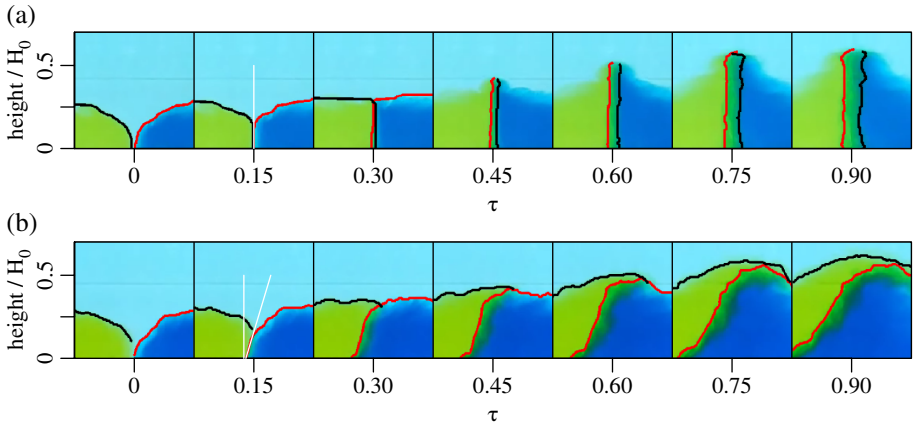

Figure 6. The front positions at and after collision for two different full-depth experiments. All heights are normalized by the total water depth, H_0, and τ is the dimensionless time. These are the same experiments shown in Figure 3 with (a) $r_g = 0.99$ and (b) $r_g = 0.33$. The red line shows the relatively heavier (blue) front and the black line the lighter (yellow) front. [Colour figure can be viewed at wileyonlinelibrary.com].

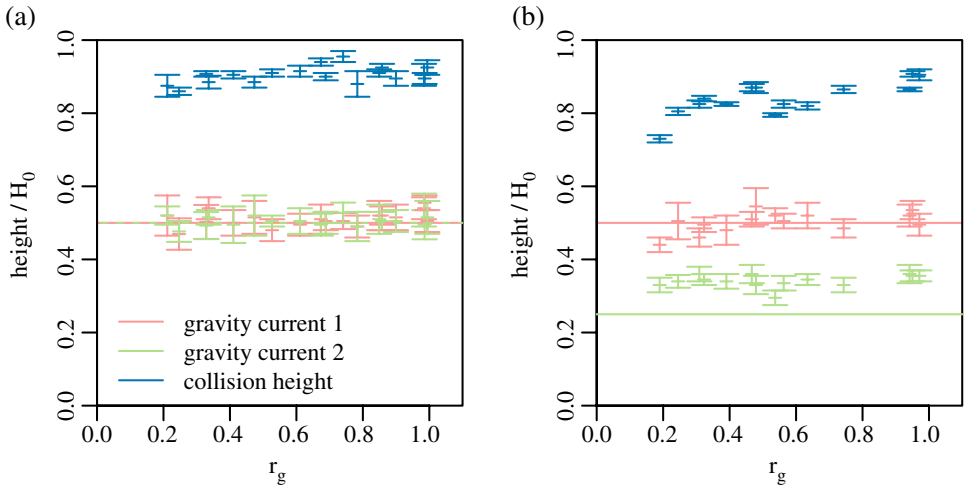

Figure 7. Pre-collision gravity current heights (light pink and green symbols) and maximum height (dark blue symbols) reached after collision against ratio r_g. All heights are normalized by the total water depth, H_0. The horizontal lines show the theoretical energy-conserving value for the height of a gravity current. Error bars show the range of measured maximum heights for each experiment. (a) Full-depth experiments and (b) half-depth experiments in the same colours. [Colour figure can be viewed at wileyonlinelibrary.com].

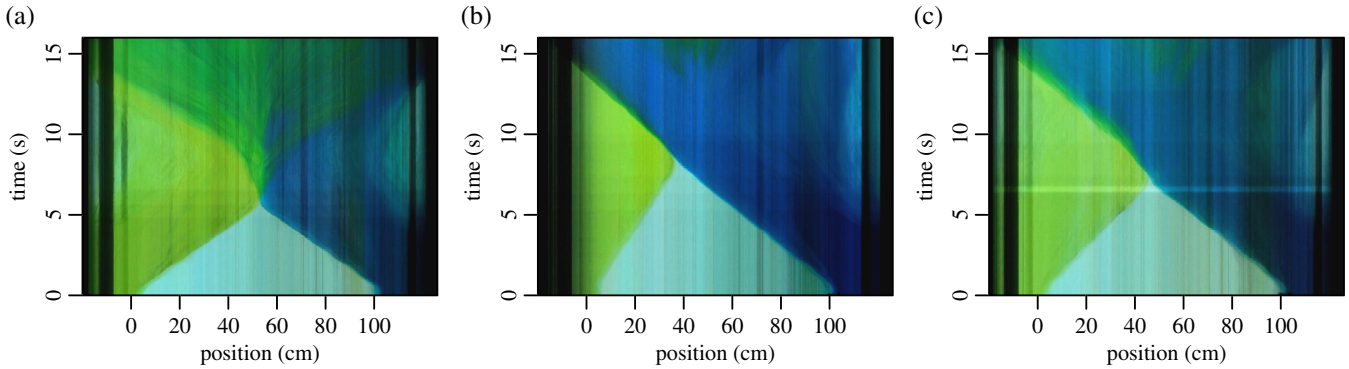

Figure 8. Hovmöller diagrams for three full-depth experiments. Two of these ((a) and (b)) are the same as shown in Figures 3 and 6. (a) $r_g = 0.99$, (b) $r_g = 0.33$ and (c) $r_g = 0.61$. [Colour figure can be viewed at wileyonlinelibrary.com].

collision front reduces density differences and prevents horizontal propagation.

For the asymmetric collisions ($r_g \leq 0.89$; dark blue marks in Figure 9) the collision front propagates in the same direction as that of the heavier current. The speed of propagation lies between 4 and 9 cm s^{-1} and increases with asymmetry of the collision and with increasing value of the characteristic speed given by Eq. (6). A model describing this post-collision propagation should include the effects of the dynamics of the gravity currents before collision, the effects of mixing and the density difference at collision. Attempts to derive such a model using the formalism explored by Shin *et al.* (2004) have been unsatisfactory.

The post-collision phase is very different in the half-depth experiments, as may be noted in the snapshots of Figure 4. In the case of equal g', the collision front is nearly vertical at the moment of impact, but soon after the higher current (dyed yellow, travelling from the left) pushes back the lower current (dyed blue, travelling from the right, Figure 4(a)). This is in contrast with the full-depth symmetric experiment in which the collision front is stationary (Figure 3(a)). The collision event for two currents of equal $g'H$ ($r_g = 0.48$) also differs from the full-depth experiments: upon impact the collision front is tilted, in a similar way to that observed in the full-depth experiments. Afterwards, a part of the heavier but lower current (dyed blue, propagating from the right) forms a new current and propagates onwards into the fluid from the other current, again as observed in the asymmetric full-depth experiments. However, part of the heavier but lower current is pushed back by the lighter fluid which, after rising vertically, sinks and continues propagating in its original direction.

The collision front is not well-defined in the half-depth experiments because of the motions generated by the lighter but higher current. For this reason, we do not extend the post-collision propagation analysis to these experiments.

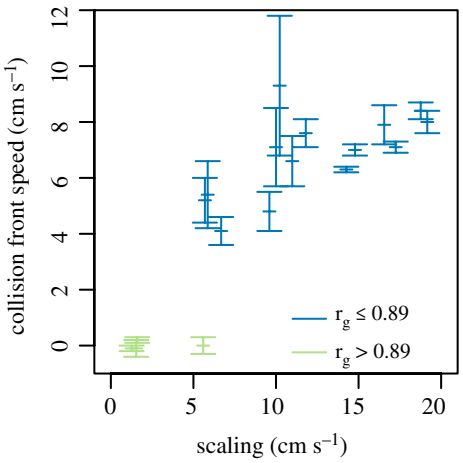

Figure 9. Experimental collision speed versus a simple scaling (Eq. (6); cm s^{-1}) for the full-depth experiments. Marks are the individual experiments. Error bars show the range of measured front speeds for each collision front. Light green marks show symmetric collisions ($r_g > 0.89$), and dark blue marks show the most asymmetric collisions ($r_g \leq 0.89$). [Colour figure can be viewed at wileyonlinelibrary.com].

4. Conclusions

Experiments using gravity currents to model two-dimensional sea and land breeze collisions have been performed. Two gravity

currents were generated from a lock-release and were allowed to collide in a rectangular channel. Both the density and the height of the currents were varied in the different experiments.

Before collision, the gravity currents propagate with a constant Froude number about 15% lower than energy-conserving theory predicts, as previous studies have also shown (e.g. Shin *et al.*, 2004). At collision a sharp front between the two currents develops. For a collision of two similar currents ($r_g \approx 1.0$, equal heights) the front is vertical and does not move horizontally. With increasing asymmetry, the front is no longer vertical but instead tilts, with the heavier gravity current propagating underneath the lighter current. The front is not steady; over time a new gravity current develops, and the collision front propagates in the same direction of the original heavier current. Mixing along the collision front decreases with asymmetry: more asymmetrical currents (lower r_g) show less mixing. The maximum height reached by the dense fluids during collision is significantly above the height of the two individual gravity currents. The collision front is less clear for two currents having different lock heights, the higher gravity current sets the direction of post-collision propagation.

In the natural environment, sea breeze circulations or convective outflows are influenced by multiple factors, and their collisions are therefore complex. These experiments were designed to give physical insights into the dynamics of the collisions, which are difficult to measure in detail in nature. Wilson *et al.* (1998) note that, for the initiation and maintenance of convection along a front, continuous strong ascending motions in the location of the developing storm are important. In the experiments, the two gravity current fronts interact, and their shapes change dramatically upon collision. There is significant ascent along the collision front, resulting in the vertical displacement of gravity current fluid. These vertical displacements have been found in all collision events and, in the natural environment, could provide the necessary trigger to overcome the convective inhibition (i.e. reach levels of positive buoyancy), setting off deep convective motions. More symmetric collisions have greater potential for initiating or enhancing deep convective motions because the horizontal position of the ascent is stationary. In the absence of ambient wind, this would create more favourable conditions for developing deep convection than the asymmetric case, where the collision front propagates and the convective forcing changes position constantly. However, even in asymmetric collisions, convection may be initiated if the lighter fluid is displaced vertically above its level of free convection.

In the current experimental set-up, the strength of vertical motions and mixing ratios could not be quantified. A new set of experiments (laboratory or numerical) could therefore provide valuable additional data. Further work might examine the energetics of kinetic and potential energy transformations during the collisions in more detail. Furthermore, the experiments could be extended to investigate gravity currents collision in a radially symmetric set-up (as in Slim and Huppert, 2004), relevant for the collision of sea breezes over (near-)circular islands. Future analysis may aim to provide a description for the post-collision horizontal propagation speeds as measured in the experiments. In nature, and in the experiments, the post-collision motions also involve reflected waves and bores, as discussed by Simpson (1997) and Shin (2001), and as can be seen in Figure 3. We have chosen to concentrate on the initial collision front here, but these other aspects would be worth further study.

Acknowledgements

The authors gratefully acknowledge the National Science Foundation (grant OCE-0824636) and the Office of Naval Research (grant N00014-09-1-0844) for their support of the 2013 WHOI Geophysical Fluid Dynamics Summer School where much of the research presented in this article was performed. The authors thank Anders Jensen for his able assistance in setting up the laboratory experiments. STG also acknowledges support from the National Aeronautics and Space Administration (grant NASA NNX14A078G).

Supporting information

The following supporting information is available as part of the online article:

Movie S1. Movie corresponding to the experiment shown in Figures 3(a), 6(a) and 8(a) on a symmetrical full-depth experiment ($r_g = 0.99$).

Movie S2. Movie corresponding to the experiment shown in Figures 3(b), 6(b) and 8(b) on an asymmetrical full-depth experiment ($r_g = 0.33$).

Movie S3. Movie corresponding to the experiment shown in Figure 4(a) on a half-depth experiment with equal g' ($r_g = 0.95$).

Movie S4. Movie corresponding to the experiment shown in Figure 4(b) on half-depth experiment with equal $g'H$ ($r_g = 0.48$).

References

Arritt RW. 1993. Effects of the large-scale flow on characteristic features of the sea breeze. *J. Appl. Meteorol.* **32**: 116–125.

Baker RD, Lynn BH, Boone A, Tao W-K, Simpson J. 2001. The influence of soil moisture, coastline curvature, and land-breeze circulations on sea-breeze-initiated precipitation. *J. Hydrometeorol.* **2**: 193–211.

Banacos PC, Schultz DM. 2005. The use of moisture flux convergence in forecasting convective initiation: Historical and operational perspectives. *Weather and Forecasting* **20**: 351–366.

Blanchard DO, López RE. 1985. Spatial patterns of convection in south Florida. *Mon. Weather Rev.* **113**: 1282–1299.

Borden Z, Meiburg E 2013. Circulation based models for Boussinesq gravity currents. *Phys. Fluids* **25**: 1–14.

Britter RE, Simpson JE. 1978. Experiments on the dynamics of a gravity current head. *J. Fluid Mech.* **88**: 223–240.

Browning KA, Morcrette CJ, Nicol J, Blyth AM, Bennett LJ, Brooks BJ, Marsham J, Mobbs SD, Parker DJ, Perry F, Clark PA, Ballard SP, Dixon MA, Forbes RM, Lean HW, Li Z, Roberts NM, Corsmeier U, Barthlott C, Deny B, Kalthoff N, Khodayar S, Kohler M, Kottmeier C, Kraut S, Kunz M, Lenfant J, Wieser A, Agnew JL, Bamber D, McGregor J, Beswick KM, Gray MD, Norton E, Ricketts HMA, Russell A, Vaughan G, Webb AR, Bitter M, Feuerle T, Hankers R, Schulz H, Bozier KE, Collier CG, Davies F, Gaffard C, Hewison TJ, Ladd DN, Slack EC, Waight J, Ramatschi M, Wareing DP, Watson RJ. 2007. The convective storm initiation project. *Bull. Am. Meteorol. Soc.* **88**: 1939–1955. https://doi.org/10.1175/BAMS-88-12-1939.

Burpee RW. 1979. Peninsula-scale convergence in the south Florida sea breeze. *Mon. Weather Rev.* **107**: 852–860.

Byers HR, Rodebush HR. 1948. Causes of thunderstorms of the Florida peninsula. *J. Meteorol.* **5**: 275–280.

Carbone RE, Conway JW, Crook NA, Moncrieff MW. 1990. The generation and propagation of a nocturnal squall line. Part I: Observations and implications for mesoscale predictability. *Mon. Weather Rev.* **118**: 26–49.

Carbone RE, Wilson JW, Keenan TD, Hacker JM. 2000. Tropical island convection in the absence of significant topography. Part I: Life cycle of diurnally forced convection. *Mon. Weather Rev.* **128**: 3459–3480.

Cenedese C, Adduce C. 2008. Mixing in a density-driven current flowing down a slope in a rotating fluid. *J. Fluid Mech.* **604**: 369–388.

Clarke RH. 1983. Fair weather nocturnal inland wind surges and atmospheric bores. Part I: Nocturnal wind surges. *Aust. Meteorol. Mag.* **31**: 133–145.

Crook NA. 2001. Understanding Hector: The dynamics of island thunderstorms. *Mon. Weather Rev.* **129**: 1550–1563.

Dai A. 2013. Experiments on gravity currents propagating on different bottom slopes. *J. Fluid Mech.* **731**: 117–141.

Droegemeier KK, Wilhelmson RB. 1985. Three-dimensional numerical modeling of convection produced by interacting thunderstorm outflows. Part II: Variations in vertical wind shear. *J. Atmos. Sci.* **42**: 2404–2414.

Fankhauser JC, Crook NA, Tuttle J, Miller LJ, Wade CG. 1995. Initiation of deep convection along boundary layer convergence lines in a semitropical environment. *Mon. Weather Rev.* **123**: 291–314.

Forbes GS, Merritt JH. 1984. Mesoscale vortices over the Great Lakes in wintertime. *Mon. Weather Rev.* **112**: 377–381.

Gahmberg M, Savijärvi H, Leskinen M. 2010. The influence of synoptic scale flow on sea breeze induced surface winds and calm zones. *Tellus* **62**: 209–217.

Gille ST, Llewellyn Smith SG. 2014. When land breezes collide: Converging diurnal winds over small bodies of water. *Q. J. R. Meteorol. Soc.* **140**: 2573–2581. https://doi.org/10.1002/qj.2322.

Gille ST, Llewellyn Smith SG, Lee SM. 2003. Measuring the sea breeze from QuikSCAT scatterometry. *Geophys. Res. Lett.* **30**: 1114. https://doi.org/10.1029/2002GL016230.

Golding B. 2005. 'Boscastle and North Cornwall post flood event study – Meteorological analysis of the conditions leading to flooding on 16 August 2004', Technical report 459. Met Office: Exeter, UK.

Hacker J, Linden PF, Dalziel SB. 1996. Mixing in lock-release gravity currents. *Dyn. Atmos. Oceans* **24**: 183–195.

Helmis CG, Asimakopoulos DN, Deligiorgi DG, Lalas DP. 1987. Observations of sea-breeze fronts near the shoreline. *Boundary-Layer Meteorol.* **38**: 395–410.

Hughes GO, Linden PF. 2016. Mixing efficiency in run-down gravity currents. *J. Fluid Mech.* **809**: 691–704. https://doi.org/10.1017/jfm.2016.696.

Kingsmill DE. 1995. Convection initiation associated with a sea-breeze front, a gust front, and their collision. *Mon. Weather Rev.* **123**: 2913–2933.

Mangia C, Martano P, Miglietta MM, Morabito A, Tanzarella A. 2004. Modelling local winds over the Salento peninsula. *Meteorol. Appl.* **11**: 231–244.

Mangia C, Schipa I, Tanzarella A, Conte D, Marra GP, Miglietta MM, Rizza U. 2010. A numerical study of the effect of sea breeze circulation on photochemical pollution over a highly industrialized peninsula. *Meteorol. Appl.* **17**: 19–31.

Maxworthy T, Leilich J, Simpson JE, Meiburg EH. 2002. The propagation of a gravity current into a linearly stratified fluid. *J. Fluid Mech.* **453**: 371–394.

Miller STK, Keim BD, Talbot RW, Mao H. 2003. Sea breeze: Structure, forecasting, and impacts. *Rev. Geophys.* **41**: 1–31.

Moncrieff MW, Liu C. 1999. Convection initiation by density currents: Role of convergence, shear, and dynamical organization. *Mon. Weather Rev.* **127**: 2455–2464.

Nicholls ME, Pielke RA, Cotton WR. 1991. A two-dimensional numerical investigation of the interaction between sea breezes and deep convection over the Florida peninsula. *Mon. Weather Rev.* **119**: 298–323.

Niino H. 1987. The linear theory of land and sea breeze circulation. *J. Meteorol. Soc. Jpn.* **65**: 901–921.

Niziol TA, Snyder WR, Waldstreicher JS. 1995. Winter weather forecasting throughout the eastern United States. Part IV: Lake effect snow. *Weather and Forecasting* **10**: 61–77.

Noonan JA, Smith RK. 1986. Sea-breeze circulations over Cape York Peninsula and the generation of Gulf of Carpentaria cloud line disturbances. *J. Atmos. Sci.* **43**: 1679–1693.

Pielke RA. 1974. A three-dimensional numerical model of the sea breezes over south Florida. *Mon. Weather Rev.* **102**: 115–139.

Ramis C, Jansá A, Alonso S. 1990. Sea breeze in Mallorca. A numerical study. *Meteorol. Atmos. Phys.* **42**: 249–258.

Rizza U, Miglietta MM, Anabor V, Degrazia GA, Maldaner S. 2015. Large-eddy simulation of sea breeze at an idealized peninsular site. *J. Marine Syst.* **148**: 167–182.

Robinson FJ, Patterson MD, Sherwood SC. 2013. A numerical modeling study of the propagation of idealized sea-breeze density currents. *J. Atmos. Sci.* **70**: 653–668.

Rottman JW, Simpson JE. 1983. Gravity currents produced by instantaneous releases of a heavy fluid in a rectangular channel. *J. Fluid Mech.* **135**: 95–110.

Sha W, Kawamura T, Ueda H. 1991. A numerical study on sea/land breezes as a gravity current: Kelvin–Helmholtz billows and inland penetration of the sea-breeze front. *J. Atmos. Sci.* **48**: 1649–1665.

Shin JO. 2001. 'Colliding gravity currents', PhD thesis. University of Cambridge: Cambridge, UK.

Shin JO, Dalziel SB, Linden PF. 2004. Gravity currents produced by lock exchange. *J. Fluid Mech.* **521**: 1–34.

Simpson JE. 1969. A comparison between laboratory and atmospheric density currents. *Q. J. R. Meteorol. Soc.* **95**: 758–765.

Simpson JE. 1997. Gravity currents in the environment and the laboratory. *J. Fluid Mech.* **352**: 376–378.

Simpson JE, Mansfield DA, Milford JR. 1977. Inland penetration of sea-breeze fronts. *Q. J. R. Meteorol. Soc.* **103**: 47–76.

Slim AC, Huppert HE. 2004. Self-similar solutions of the axisymmetric shallow-water equations governing converging inviscid gravity currents. *J. Fluid Mech.* **506**: 331–355.

Soderholm J, McGowan H, Richter H, Walsh K, Weckwerth T, Coleman M. 2015. The Coastal Convective Interactions Experiment (CCIE): Understanding the role of sea breezes for hailstorm hotspots in Eastern Australia. *Bull. Am. Meteorol. Soc.* **97**: 1687–1698.

Sumner G, Ramis C, Guijarro JA. 1993. The spatial organization of daily rainfall over Mallorca, Spain. *Int. J. Climatol.* **13**: 89–109.

Tijm ABC, van Delden AJ, Holtslag AAM. 1999. The inland penetration of sea breezes. *Contrib. Atmos. Phys.* **72**: 317–328.

Wapler K, Lane TP. 2012. A case of offshore convective initiation by interacting land breezes near Darwin, Australia. *Meteorol. Atmos. Phys.* **115**: 123–137.

Warren RA. 2014. 'Quasi-stationary convective systems in the UK', PhD thesis. University of Reading: Reading, UK.

Wilson JW, Schreiber WE. 1986. Initiation of convective storms at radar-observed boundary-layer convergence lines. *Mon. Weather Rev.* **114**: 2516–2536.

Wilson JW, Crook NA, Mueller CK, Sun J, Dixon M. 1998. Nowcasting thunderstorms: A status report. *Bull. Am. Meteorol. Soc.* **79**: 2079–2099.

Wulfmeyer V, Behrendt A, Kottmeier C, Corsmeier U, Barthlott C, Craig GC, Hagen M, Althausen D, Aoshima F, Arpagaus M, Bauer H-S, Bennett L, Blyth A, Brandau C, Champollion C, Crewell S, Dick G, DiGirolamo P, Dorninger M, Dufournet Y, Eigenmann R, Engelmann R, Flamant C, Foken T, Gorgas T, Grzeschik M, Handwerker J, Hauck C, Höller H, Junkermann W, Kalthoff N, Kiemle C, Klink S, König M, Krauss L, Long CN, Madonna F, Mobbs S, Neininger B, Pal S, Peters G, Pigeon G, Richard E, Rotach MW, Russchenberg H, Schwitalla T, Smith V, Steinacker R, Trentmann J, Turner DD, van Baelen J, Vogt S, Volker H, Weckwerth T, Wernli H, Wieser A, Wirth M. 2011. The Convective and Orographically induced Precipitation Study (COPS): The scientific strategy, the field phase, and research highlights. *Q. J. R. Meteorol. Soc.* **137**: 3–30.

Xian Z, Pielke RA. 1991. The effects of width of landmasses on the development of sea breezes. *J. Appl. Meteorol.* **30**: 1280–1304.

Yan H, Anthes RA. 1987. The effect of latitude on the sea breeze. *Mon. Weather Rev.* **115**: 936–956.

